scientific reports

Check for updates

OPEN

Lattice modulations in the double charge density wave system $Er_5Ir_4Si_{10}$

V. Petkov[1]✉, A. Zafar[1], M. Jakhar[1,2], S. Shastri[3], L. Gallington[3], A M Milinda Abeykoon[4] & B. Aoun[5]

Using total and resonant X-ray scattering combined with large-scale structural modeling, we investigate the lattice modulations in $Er_5Ir_4Si_{10}$, which hosts coexisting incommensurate and commensurate charge-density waves (CDWs). We find that long-range CDW order emerges from a precursor state characterized by local lattice distortions, as evidenced by pronounced diffuse scattering in the diffraction data. These distortions involve displacements of Er, Ir, and Si atoms from their room-temperature crystallographic positions that become increasingly correlated upon cooling, producing substantial changes in the local bonding network at low temperatures. Density-functional-theory calculations performed directly on the experimentally refined structural models reveal an extended soft/unstable phonon manifold on the q_z=1/2 Brillouin-zone face in the precursor phase that includes the experimentally observed CDW modulation wave vector. Upon entering the CDW phase, the strongest phonon feature occurs at the corresponding physical wave vector, suggesting selection of the CDW modulation from this pre-existing soft manifold. The calculations also reveal a partial suppression of the electronic density of states at the Fermi level, consistent with earlier muon spin relaxation measurements. Our results identify correlated local lattice distortions and their associated phonon instabilities as important ingredients in the formation and evolution of CDW order in $Er_5Ir_4Si_{10}$ and support the broader view that precursor lattice distortions can play a significant role in the emergence of complex electronic phases in quantum materials.

Charge density waves (CDWs) are a quantum phenomenon arising from the collective behavior of interacting electrons and phonons, leading to coupled charge modulations and lattice distortions below a transition temperature, T_{CDW}[1–5]. The onset of the CDW state is accompanied by significant changes in the electronic properties arising from a concurrent reconstruction of the Fermi surface[6–13]. However, directly identifying the lattice distortions that precede or accompany CDW formation has proven challenging. As a result, key aspects of the CDW formation mechanism and its connection to anomalous electronic transport remain poorly understood. Materials hosting multiple or coexisting CDW phases provide a unique opportunity to address these questions by elucidating the roles of lattice distortions, electron-lattice coupling, and symmetry-breaking processes.

A representative example of such materials is the $RE_5Ir_4Si_{10}$ family of compounds[14–24]. The non-magnetic end member $Lu_5Ir_4Si_{10}$ exhibits competing CDW and superconducting orders below $T_{CDW} \approx 85$ K and $T_{SC} \approx 4$ K, respectively[25–27]. In contrast, magnetic members with RE = Er, Ho, and Dy display coexisting CDW and antiferromagnetic (AFM) orders below, respectively, $T_{CDW} \approx 200$ K and a Néel temperature $T_N \approx 5$ K[28–34]. Among this family, $Er_5Ir_4Si_{10}$ is unique because it undergoes two CDW phase transitions involving coexisting incommensurate (I) and commensurate (C) CDWs. Single-crystal diffraction studies[17,23,35] have shown that incommensurate and commensurate CDWs with modulation wave vectors $q_{I-CDW} = (0,0,1/4 \pm \delta)$ and $q_{C-CDW} = (0,0,1/2)$, respectively, emerge simultaneously below $T_{I/C-CDW} \approx 155$ K. Upon further cooling, the incommensurate CDW evolves into a purely commensurate superstructure with modulation vector $q_{I-CDWC} = (0,0,1/4)$ below $T_{C-CDW} \approx 55$ K. This phase persists into an antiferromagnetically ordered state that develops below $T_N \approx 3$ K[29,30]. It has been proposed that the $q_{C-CDW} = (0,0,1/2)$ modulation originates from a second-order phase transition at $T_{I/C\text{-}CDW}$ that doubles the unit cell, giving rise to an incommensurate CDW with wave vector

[1]Department of Physics, Central Michigan University, Mt. Pleasant 48858, MI, USA. [2]Inter-University Accelerator Center, Aruna Asaf Ali Marg, New Delhi, India. [3]X-Ray Science Division, Advanced Photon Source, Argonne National Laboratory, Lemont, IL 60439, USA. [4]Photon Sciences Division, Brookhaven National Laboratory, Upton, NY 11973, USA. [5]fullrmc LLC, Dallas, TX 75002, USA. ✉email: petko1vg@cmich.edu

q_{I-CDW} = (0,0,1/4 ± δ) defined with respect to the doubled unit cell. Upon cooling, the δ decreases and goes to zero at the lock-in transition temperature T_{C-CDW}[23].

As typical for CDW systems, the high-temperature phase without long-range CDW order is metallic. However, the electrical resistivity ρ exhibits a highly nonlinear temperature dependence extending well below $T_{I/C-CDW}$ while retaining metallic character[20]. This behavior indicates that charge modulations in $Er_5Ir_4Si_{10}$ open a gap over only part of the Fermi surface rather than driving a full metal-insulator transition. A reduction of the density of states (DOS) at the Fermi level, E_f, due to the partial gap opening has been suggested based on muon relaxation time measurements[36]. The resistivity anisotropy has been found to be relatively small (~ 1:2) compared with canonical quasi-two-dimensional CDW systems such as $NbSe_3$, where it reaches ~ 1:20[37], suggesting that the charge modulations develop along more than one crystallographic direction. A pronounced peak in the specific heat and a large entropy change have been observed at $T_{I/C-CDW}$, suggesting the presence of substantial electron-phonon coupling[23].

Interestingly, prior pressure- and magnetic-field-dependent studies have revealed distinct responses of the CDW states in $Er_5Ir_4Si_{10}$ to external stimuli in comparison with non-magnetic $Lu_5Ir_4Si_{10}$. In $Er_5Ir_4Si_{10}$, $T_{I/C-CDW}$ has been found to be essentially pressure independent, whereas T_{C-CDW} appeared strongly suppressed with increasing pressure. This behavior contrasts with that of $Lu_5Ir_4Si_{10}$ where the single CDW transition decreases monotonically with pressure. Magnetic-field measurements on $Er_5Ir_4Si_{10}$ have further shown that both $T_{I/C-CDW}$ and T_{C-CDW} are robust and remain largely unaffected by magnetic field, whereas the antiferromagnetic ordering temperature T_N appeared reduced. Studies have also found that, at low temperatures, $Er_5Ir_4Si_{10}$ exhibits negative magnetoresistance, opposite in sign to that observed with $Lu_5Ir_4Si_{10}$[38].

The prevailing view is that the unusual physical properties of $Er_5Ir_4Si_{10}$ are closely linked to its distinctive crystal structure. At room temperature the compound crystallizes in the tetragonal space group P4/*mbm*, in which two types of atomic layers are stacked along the crystallographic *c* axis. One layer contains Er, Ir, and Si atoms, whereas the other is composed only of Er and Si atoms. Within each layer, the atoms form interconnected networks of squares, rhombuses, and octagons, as illustrated in Fig. 1(a, b). Extensive single-crystal diffraction studies have not detected changes in the average tetragonal lattice symmetry down to $T = 3$ K. Nor have they identified clear lattice distortions associated with the onset of CDW order below $T_{I/C-CDW}$. Consequently, definitive evidence for the roles of the different atomic species in the CDW formation, as well as the pattern of lattice distances that emerges when CDW order sets in, remains lacking. This lack of microscopic structural information has limited a comprehensive understanding of the mechanism underlying the CDW formation and the connection between the CDW order and the anomalous electronic properties in $Er_5Ir_4Si_{10}$.

Here, using total and resonant X-ray scattering combined with large-scale structural modeling, we show that $Er_5Ir_4Si_{10}$ exhibits lattice distortions already well above $T_{I/C-CDW}$. The distortions involve displacements of Er, Ir,

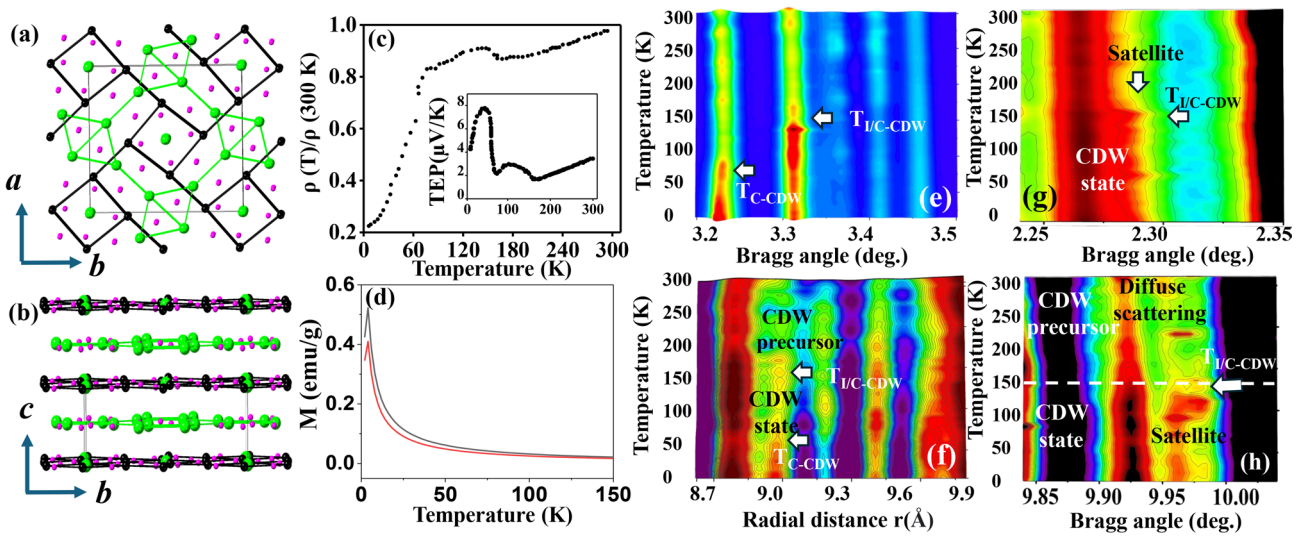


Fig. 1. (**a**, **b**) Projections of the tetragonal S.G. P4/*mbm* crystal structure of $Er_5Ir_4Si_{10}$, where the unit cell is outlined by a thin gray line. The structure consists of two types of atomic layers stacked along the crystallographic *c* axis. Er, Ir, and Si atoms are represented by green, black, and magenta circles, respectively. (**c**) Temperature dependence of the normalized electrical resistivity (ρ) and thermoelectric power (TEP), adapted from Refs[20,21]. Both quantities exhibit pronounced nonlinearities in the vicinity of $T_{I/C-CDW}$ and T_{C-CDW}. (**d**) Field-cooled (red) and zero-field-cooled (black) magnetization data. The magnetization exhibits a peak at the Néel temperature $T_N \approx 4$K, where the material undergoes a transition to an antiferromagnetic state. (**e**) Synchrotron X-ray diffraction (XRD) and (**f**) atomic pair distribution function (PDF) intensity maps for $Er_5Ir_4Si_{10}$. Arrows highlight nonlinearities in the temperature evolution of selected XRD and PDF peaks, appearing above and near $T_{I/C-CDW} \approx 150$ Kand at $T_{C-CDW} \approx 55$ K. (**g**,**h**) Superstructure satellites appearing when the temperature is reduced below $T_{I/C-CDW}$. Their intensity is about 10^{-2} weaker than that of the strongest Bragg peak in the XRD pattern.

and Si atoms from their room-temperature crystallographic positions, which become increasingly correlated upon cooling, eventually leading to significant changes in the local bonding network below $T_{I/C\text{-}CDW}$. Density functional theory (DFT) calculations performed directly on the experimentally derived structural models reveal an extended soft/unstable phonon manifold on the q_z = 1/2Brillouin-zone face in the precursor phase that contains the experimentally observed CDW modulation vector, $q_{C\text{-}CDW}$ = (0,0,1/2). Upon entering the I/C-CDW phase, the strongest phonon feature occurs at the corresponding physical wave vector, suggesting selection of the CDW modulation from this pre-existing soft manifold. The calculations also reveal a partial suppression of the electronic density of states at the Fermi level. Taken together, our results suggest that precursor lattice distortions and their associated phonon instabilities make an important contribution to the emergence of CDW order in $Er_5Ir_4Si_{10}$.

Results and discussion

Sample preparation and properties characterization

Polycrystalline $Er_5Ir_4Si_{10}$ samples were synthesized by arc melting the constituent elements in an argon atmosphere. The arc-melted ingots were subsequently annealed at 900 °C for 10 days in a sealed quartz tube to ensure chemical homogeneity. In-house X-ray diffraction (XRD) measurements confirmed that the annealed material is single phase.

Electrical resistivity and thermoelectric power data reported in previous studies[20,21] are summarized in Fig. 1(c). The resistivity, ρ, decreases slightly as the material is cooled from room temperature to approximately 250 K and then remains nearly constant upon further cooling down to $T_{I/C\text{-}CDW}$. At this temperature, ρ increases by about 5%, signaling partial charge localization associated with the onset of I/C-CDW order. The resistivity then remains nearly constant in the temperature interval between $T_{I/C\text{-}CDW}$ and $T_{C\text{-}CDW}$. Upon approaching the C-CDW phase, however, ρ decreases rapidly, indicating significantly enhanced metallic behavior compared with the room temperature state. Thermal conductivity data reported previously[21], summarized in Fig. S1 of the Supplemental Material[39], also exhibit a strongly non-linear temperature dependence in the vicinity of both $T_{I/C\text{-}CDW}$ and $T_{C\text{-}CDW}$. Our magnetization data obtained using a Physical Property Measurement System are shown in Fig. 1(d). They are consistent with earlier studies[38], displaying a pronounced peak at approximately 4 K, which marks the onset of antiferromagnetic order.

Use of total x-ray scattering in CDW structure studies

The superstructure associated with CDW is commonly determined by single-crystal diffraction through the observation and analysis of weak satellite reflections that appear at wave vectors offset from the fundamental Bragg peaks by the CDW modulation vector q_{CDW}. Careful measurement of the satellite peak positions and intensities enables refinement of the modulated structure and determination of the modulation vector, symmetry, and amplitude of the lattice distortion. Temperature-dependent diffraction measurements further allow the evolution of the CDW order parameter, lock-in transitions, and commensurability effects to be tracked through changes in the satellite peak intensity and position[3,40–42]. When the satellite peaks are limited and/or poorly defined, however, the CDW superstructure, in particular the nature and amplitude of the lattice distortions, may be difficult to determine, as is the case with $Er_5Ir_4Si_{10}$. In such cases, an alternative approach based on the analysis of atomic pair distribution functions (PDFs), obtained from total x-ray scattering experiments, has proven useful. In contrast to single-crystal diffraction, which focuses on superlattice satellite reflections whose intensities are typically less than 1% of those of the main Bragg peaks, total x-ray scattering utilizes the entire diffraction signal, as all of its components—including Bragg peaks, satellites, and diffuse scattering—are sensitive to emergent lattice distortions[43]. Moreover, the data are analyzed in real space in the form of PDFs, which, similarly to the widely used Patterson function in crystallography, directly reflect all interatomic distances in the studied material. Thus, PDFs obtained from total x-ray scattering data via Fourier transformation have enhanced sensitivity to lattice distortions associated with short- and/or long-range CDWs. Representative examples include PDF studies of distortions in the Te nets in the incommensurate CDW phase of $CeTe_3$[44], the emergence of a superstructure of Ta clusters in the CDW phase of 2 H-$TaSe_2$[45], atomic displacement modes in the CDW phases of quasi-one-dimensional $NbTe_4$[46], and the temperature- and composition-dependent evolution of lattice distortions and CDWs in the $RENiC_2$ system (RE = Dy, Tb, Gd, and Sm)[47]. Additional examples include studies on the three-dimensional lattice modulations in $LuIr_3Si_5$[48] and the evolution of symmetry breaking across the incommensurate, nearly commensurate, and commensurate CDW phases of 1T-TaS_2[49]. Because total x-ray scattering experiments are typically performed using high-energy x-rays, the resulting diffraction patterns are compressed toward lower wave vectors, leading to reduced resolution of satellite reflections. As a result, it is difficult to determine the superstructure symmetry from PDF analysis alone. Consequently, PDF studies often benefit from prior high-resolution single-crystal diffraction results, particularly for determining the periodicity of the superstructure. In the present work, we take advantage of previous single-crystal studies indicating that the tetragonal unit cell of $Er_5Ir_4Si_{10}$ doubles below $T_{I/C\text{-}CDW}$.

Total x-ray scattering experiments

Total x-ray scattering experiments were performed at the 28-ID-1 beamline of the National Synchrotron Light Source II (NSLS-II) at Brookhaven National Laboratory using x-rays with an energy of 74.46 keV and a PerkinElmer area detector. The sample was mounted in a liquid-helium cryostat, and data were collected while cooling from 300 K to 10 K in steps of 5 K. Intensity-colored maps of the diffraction patterns are shown in Fig. 1(e). The patterns display Bragg peaks, which change significantly at $T_{I/C\text{-}CDW}$, satellite reflections that emerge below $T_{I/C\text{-}CDW}$, and fluctuating diffuse scattering above $T_{I/C\text{-}CDW}$ (Fig. 1(g, h)). Total atomic PDFs were obtained from the experimental XRD patterns using standard data-reduction procedures[50]. The resulting PDFs are presented in Figs. 1(f) over a selected range of interatomic distances. Some atomic pair correlations,

for example near 9 Å, appear above $T_{I/C\text{-}CDW}$ and gradually strengthen while others, for example near 9.3 Å, become weaker with decreasing temperature. In contrast, certain correlations (e.g., near 8.8 Å) remain virtually unchanged from room temperature down to 10 K. These observations indicate that the crystal lattice undergoes a gradual, partial reconstruction over an extended range of interatomic distances, with this process beginning well above the onset of CDW order. In this sense, the partial reconstruction above $T_{I/C\text{-}CDW}$ may be viewed as a precursor to the emergence of the CDW state. Notably, such a reconstruction is unlikely to arise solely from conventional changes in thermally induced atomic vibrations, which would be expected to affect the PDF peaks more uniformly than observed in $Er_5Ir_4Si_{10}$.

The total PDFs, however, contain contributions from six distinct pair correlations among the constituent atoms: Er-Er, Er-Ir, Er-Si, Ir-Ir, Ir-Si, and Si-Si[43,51]. These contributions overlap strongly in the measured PDFs [Fig. 2(a)], making an unambiguous interpretation of the local structural changes challenging. To enhance sensitivity to atomic correlations involving Ir atoms, which are expected to play an important role in CDW-related lattice distortions, we performed resonant X-ray scattering experiments[52,53] at the Ir K edge (76.111 keV). These measurements were carried out at beamline 1-ID-E of the Advanced Photon Source (APS) at Argonne National Laboratory using a Pilatus3X CdTe 2 M detector[54]. An Oxford 800-series Cryostream system was used for temperature control. Data were collected at several temperatures between 300 and 100 K, spanning the $T_{I/C\text{-}CDW}$ transition. At each temperature, two diffraction patterns were measured: one at 25 eV below the Ir K edge and the other at 525 eV below the edge. Representative diffraction patterns are shown in Fig. 2(c). From the intensity difference between these two patterns, Ir-differential PDFs were derived following the procedures described in Refs[53,55]. The resulting Ir-differential PDFs contain only pair correlations involving Ir atoms, namely Ir-Ir, Ir-Er, and Ir-Si correlations [Fig. 2(b)], thereby providing element-specific structural information complementary to that obtained from the total PDFs [Figs. 2(d, e)]. The Ir-differential PDFs also exhibit a clear temperature dependence [Fig. 2(f)]. Consequently, they provide an important additional experimental constraint for the large-scale structural modeling described below.

Temperature evolution of the average crystal structure from analysis of Bragg peaks

The average crystal structure of $Er_5Ir_4Si_{10}$ was assessed through Rietveld refinement of the experimental XRD data using the GSAS-II software package[56]. Representative refinement results are presented in Fig. 3(a-c). As shown in the figure, a structural model based on the tetragonal space group P4/*mbm* reproduces the diffraction data well over a wide temperature range encompassing the room temperature and I/C-CDW phases of the material. These results confirm prior single-crystal studies showing that the average crystallographic symmetry does not change when the CDW order sets in[23]. The refined lattice parameters and unit-cell volume are summarized

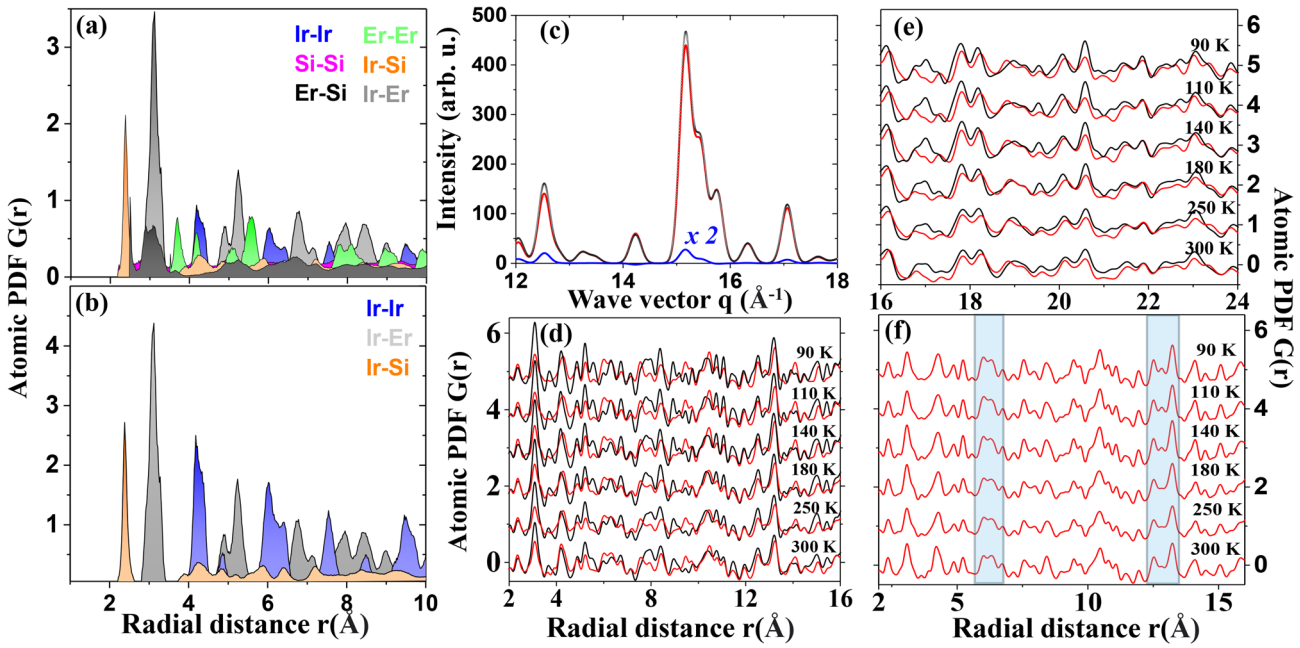


Fig. 2. Partial atomic correlations contributing to the (**a**) total and (**b**) Ir-differential PDFs of $Er_5Ir_4Si_{10}$. As shown, correlations involving Ir atoms (Ir-Ir, Ir-Er, and Ir-Si) strongly overlap with correlations not involving Ir (Er-Er, Er-Si, and Si-Si) in the total PDF. In contrast, these non-Ir correlations are absent in the Ir-differential PDF, which contains only correlations involving Ir atoms. (**c**) XRD patterns for $Er_5Ir_4Si_{10}$ measured at photon energies 25 eV (red) and 525 eV (black) below the Ir K edge. Their difference, multiplied by a factor of two, is also shown (blue). (**d**) Low-*r* region of the total (black) and Ir-differential (red) PDFs measured at different temperatures. (**e**) High-*r* region of the total (black) and Ir-differential (red) PDFs measured at different temperatures. (**f**) Expanded view of the low-*r* region of the Ir-differential PDFs. Light-blue shaded rectangles highlight systematic temperature-dependent changes in the Ir-involving pair correlations.

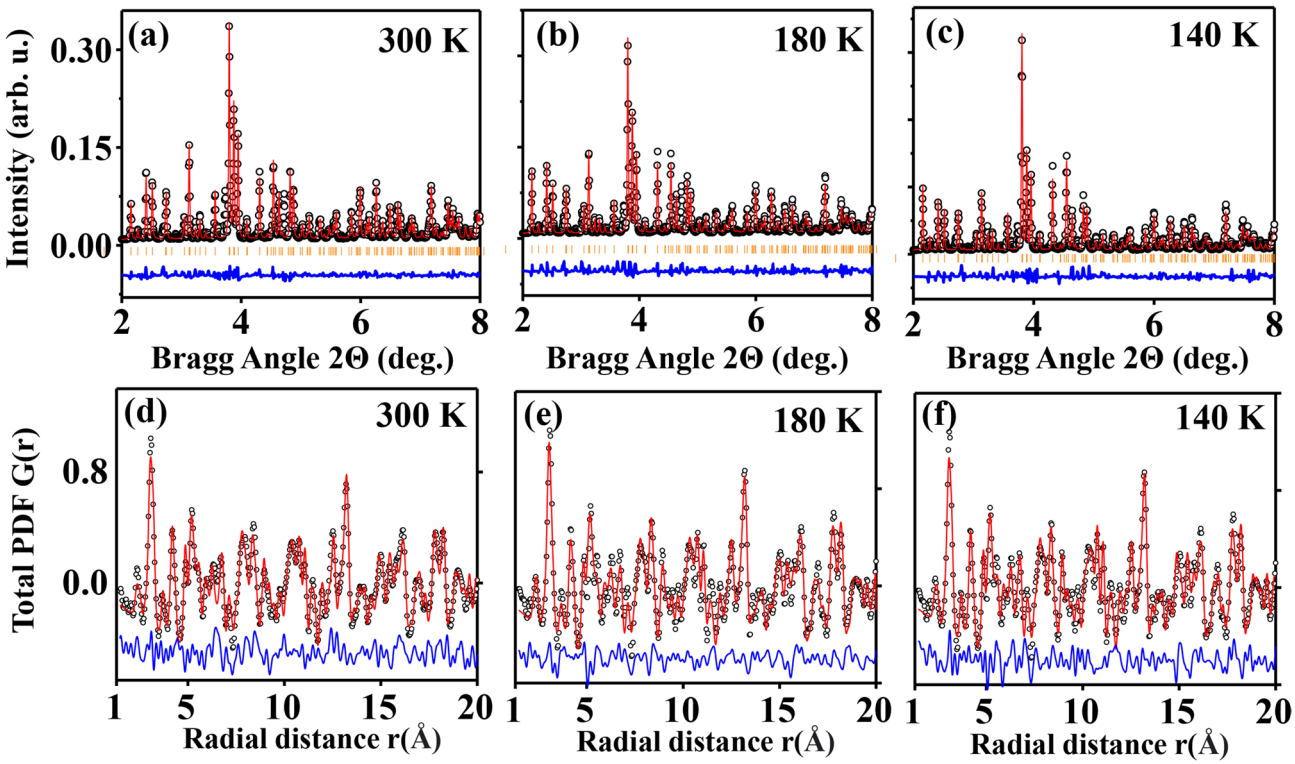


Fig. 3. (Upper row) Rietveld refinements (red lines) of XRD patterns (symbols) for $Er_5Ir_4Si_{10}$ obtained at different temperatures. Vertical orange bars mark the positions of Bragg peaks. The goodness-of-fit factor is approximately 9% for all refinements. (Lower row) Fits based on a single crystallographic unit-cell model (red lines) to total PDFs (symbols) for $Er_5Ir_4Si_{10}$ obtained at different temperatures. The goodness-of-fit factor is approximately 25%. For clarity, the residual differences between the experimental and calculated data (blue lines) are vertically offset.

in Fig. 4. Their temperature evolution exhibits nonlinearities near $T_{\text{I/C-CDW}}$ and T_{CDW}, indicating that lattice distortions significantly affect the average crystal structure. However, the precise nature of these distortions cannot be determined from analysis of Bragg diffraction peaks alone.

Temperature evolution of the local structure from small-unit-cell-based PDF-guided modeling

To gain insight into the impact of lattice distortions on the local crystal structure, we performed PDF analysis using the same single-unit-cell structural model with space group $P4/mbm$. The PDF analysis was carried out using the PDFgui software package[60]. The refinements were performed over a real-space range of 2–20 Å to obtain reliable structural parameters. This fitting range enables a uniform description of lattice distortions that are local at room temperature but become progressively more correlated upon cooling, eventually giving rise to a superstructure spanning several crystallographic unit cells. Representative fits are shown in Fig. 3(d-f). Overall, the model reproduced the experimental PDF data reasonably well. The refined lattice parameters and unit-cell volume obtained from the PDF analysis are shown in Fig. 4. In contrast to the Rietveld results, their temperature dependence exhibits pronounced inflection points near $T_{\text{I/C-CDW}}$ and $T_{\text{C-CDW}}$. A weak inflection is also observed near 250 K. These results indicate that lattice distortions emerging above $T_{\text{I/C-CDW}}$ continue to evolve upon cooling, significantly affecting the local crystal structure. Nevertheless, noticeable residual differences between the experimental and calculated PDFs remain. These discrepancies suggest that, at the local level, the lattice distortions associated with CDW order in $Er_5Ir_4Si_{10}$ do not fully conform to the crystallographic space-group symmetry $P4/mbm$, indicating that this symmetry is locally broken.

Temperature evolution of lattice distortions from large-scale PDF-guided modeling

To obtain a more detailed picture of the temperature-dependent local lattice distortions, we refined large-scale atomic models against both the experimental total PDFs and Ir-differential PDFs obtained above and below $T_{\text{I/C-CDW}}$ using the reverse Monte Carlo (RMC) technique[45,47,61,62]. The calculations were performed using the fullrmc software package[63]. Initial atomic configurations containing approximately 22,000 atoms (corresponding to a $6a$ x $6a$ x $16c$ simulation box with dimensions of about 75 Å × 75 Å × 70 Å) were constructed for the room-temperature, 180 K, and 140 K phases of $Er_5Ir_4Si_{10}$. These starting configurations were generated using the tetragonal lattice parameters (a and c) and atomic positions obtained from the single-unit-cell PDF refinements shown in Fig. 3(d), 3(e), and 3(f), respectively. The large size of the simulation cells enabled us to explore lattice

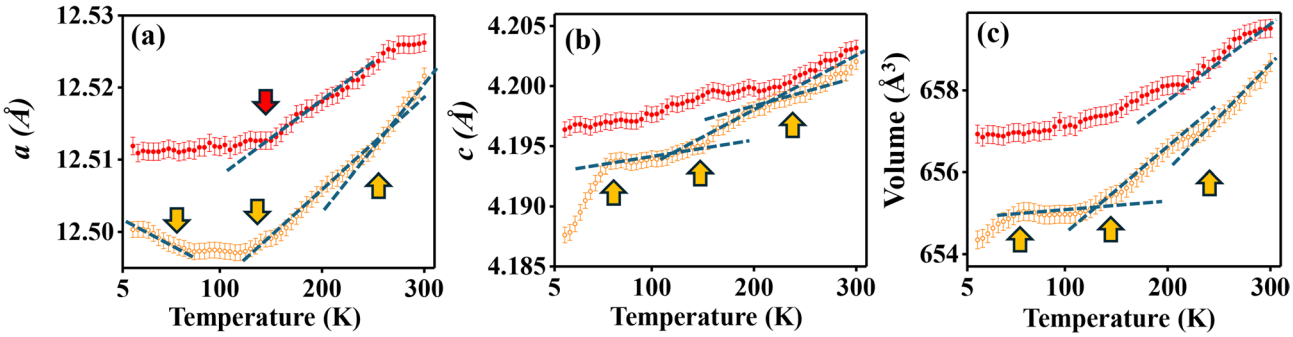


Fig. 4. Temperature dependence of the **(a)** and **(c)** lattice parameters and unit cell volume for $Er_5Ir_4Si_{10}$ obtained from Rietveld refinements (red symbols) and single-unit-cell PDF fits (orange symbols). As observed in many CDW materials[47,57–59], the lattice parameters derived from Rietveld and PDF analyses differ significantly due to the presence of local lattice distortions. Notably, the PDF analysis yields a smaller unit-cell volume than that obtained from the Rietveld refinements, indicating that the local structure of $Er_5Ir_4Si_{10}$ is more compressed than the average bulk structure. All PDF-derived quantities exhibit pronounced nonlinearities near $T_{I/C\text{-}CDW} \approx 150$ K and $T_{C\text{-}CDW} \approx 55$ K (indicated by arrows), coinciding with the onset and evolution of CDW order. A nonlinearity is also observed near 250 K, consistent with an incipient lattice instability. Dashed lines are used as guides to the eye.

distortions extending up to 37 Å (half the size of the simulation box), irrespective of whether the distortions were periodic or not. During the RMC refinement, all atoms were initially allowed to move with a step size of 0.02 Å, which was reduced to 0.01 Å during the final stages of the modeling. Atomic displacements were not constrained to occur along specific crystallographic directions; however, interatomic distance constraints were imposed to prevent atoms from approaching closer than the sum of their respective atomic radii. The refinement process was terminated once no further improvement in the agreement between the calculated and experimental total and Ir-differential PDFs could be achieved. To assess the robustness and reproducibility of the refinements, the RMC simulations were repeated by varying (i) the fitting ranges, (ii) the number of RMC steps, (iii) the relative weights assigned to the total and Ir-differential PDFs, (iv) the model sizes (including 60 Å × 60 Å × 60 Å and 80 Å × 80 Å × 80 Å models), and (v) the initial amplitudes of the atomic displacements from their high-symmetry positions. Several independent RMC refinements of the model atomic configurations were performed using different combinations of these modeling parameters. The resulting independently converged configurations produced statistically equivalent fits to the experimental data and yielded consistent pair-distance distributions, coordination environments, and atomic-displacement correlations. Three representative independently converged 22,000-atom configurations were selected as the final structural models, and the reported structural parameters were obtained by averaging the corresponding quantities extracted from these configurations. Although individual RMC configurations are not expected to be mathematically unique, the reproducibility of these structural features across independent refinements indicates that they are robust and well constrained within the resolution of the experimental data and the imposed modeling constraints. Results from converged RMC fits are shown in Fig. 5. Their quality is superior to that of the single-unit-cell PDF refinements presented in Fig. 3(d-f). Notably, although the structural models were refined exclusively against real-space PDF data, they also reproduce the emergence of weak satellite reflections in the reciprocal-space XRD data below $T_{I/C\text{-}CDW}$ (see Fig. S2), providing an independent validation of the models' reliability.

Projections of the RMC-refined atomic configurations onto selected crystallographic planes, obtained without imposing local crystallographic symmetry constraints, are shown in Fig. 6. Projections of the electron density distribution onto the same planes, calculated from the RMC-refined models, are also shown. The atomic pair distances within orthogonal crystallographic planes of the tetragonal structure of $Er_5Ir_4Si_{10}$ exhibit significant temperature evolution. This evolution originates from correlated displacements of Er, Ir, and Si atoms from their room-temperature crystallographic positions, which begin to develop well above $T_{I/C\text{-}CDW}$ and are likely responsible for the changes in the PDF peaks (see Fig. 1(f)) observed both above and below that temperature. The displacements alter the pattern of bonding distances in different crystallographic planes, highlighting the three-dimensional character of the lattice modulations in the CDW state of $Er_5Ir_4Si_{10}$. At the same time, the spatial distribution of the electron density evolves with temperature, consistent with the presence of substantial electron-lattice interactions. Changes in the distances between Si atoms are highlighted in Fig. 7. While some Er-Er (Fig. 6(a-c)) and Ir-Ir (Fig. 6(g-i)) distances change by approximately 0.01–0.08 Å, some near-neighbor Si-Si distances are seen to vary by as much as 0.2 Å, indicating that the CDW lattice modulations are particularly pronounced for Si atoms. In this respect, $Er_5Ir_4Si_{10}$ resembles $Gd_2Os_3Si_5$[64], where displacements of Si atoms have also been found to dominate the CDW lattice modulations.

Electron structure of $Er_5Ir_4Si_{10}$ from DFT calculations based on PDF-derived structure data

It is well established that experimental crystal structures provide useful structural models for electronic-structure calculations. To capture the temperature evolution of the electronic structure, we therefore performed density-functional-theory (DFT) calculations using structural models representative of three temperatures: room temperature, 180 K, and 140 K, with the latter two lying just above and below the $T_{I/C\text{-}CDW}$ phase transition.

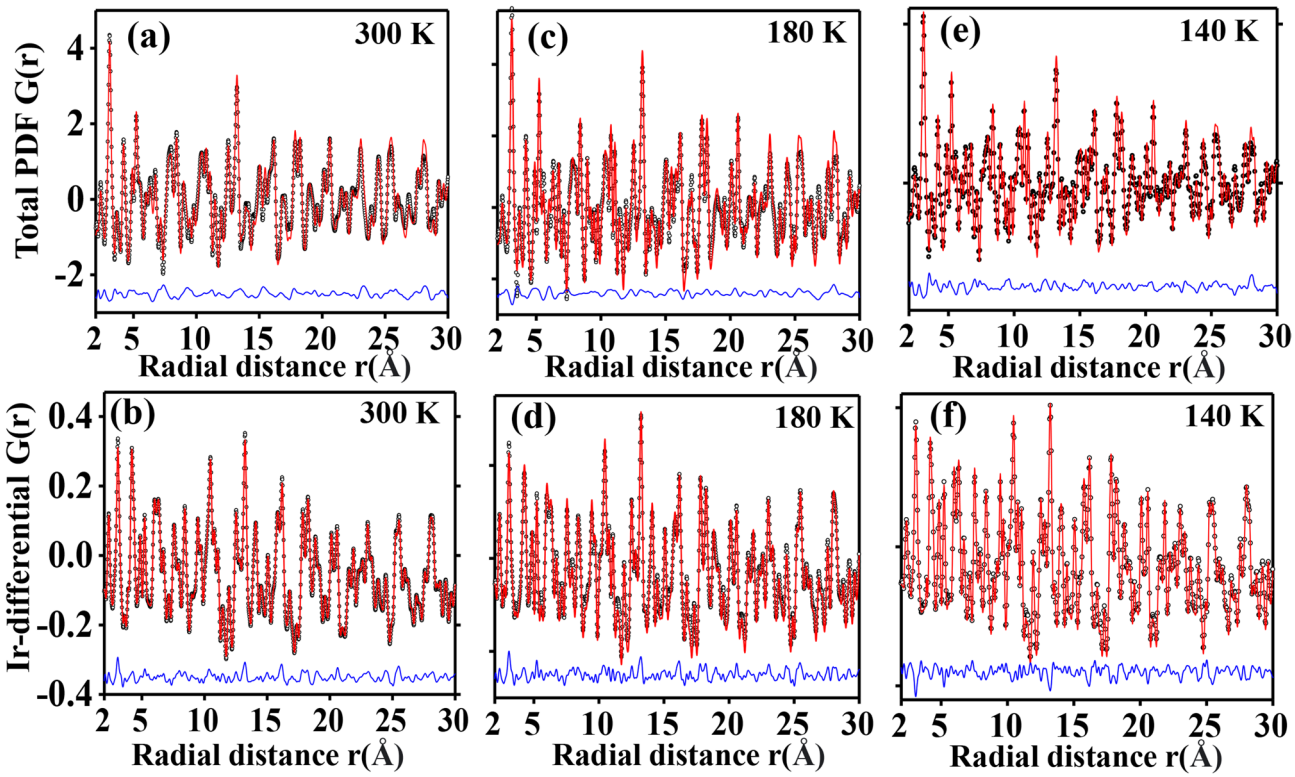


Fig. 5. Reverse Monte Carlo (RMC) fits (red lines) to (upper row) total PDFs and (lower row) Ir-differential PDFs for $Er_5Ir_4Si_{10}$ obtained at different temperatures. The goodness-of-fit factor is approximately 7% for the total PDFs and 10% for the Ir-differential PDFs. For clarity, the residual differences between the experimental and calculated data (blue lines) are vertically offset. To capture possible longer-range lattice distortions, the fit range extends over distances comparable those in a 2*a* x 2*a* x 6*c* supercell, where the *a* and *c* are the lattice parameters derived from the fits shown in Fig. 3(d-f). This includes interatomic correlations within the 1*a* x 1*a* x 2*c* supercells associated with the I/C-CDW phase.

The structural basis for the room-temperature structurally distorted CDW precursor phase of $Er_5Ir_4Si_{10}$ was constructed by folding the corresponding 22,000-atom RMC-refined model into a tetragonal $1a \times 1a \times 1c$ unit cell used to generate the initial atomic configuration, without imposing local symmetry constraints on the atomic positions within the cell. In this procedure, each of the 38 atomic positions in the resulting unit cell corresponds to the geometric center of the projected positions of 576 equivalent atoms in the 22,000-atom RMC-refined configuration (See Table S1). The structural model used for the DFT calculations at 180 K was constructed in the same manner (see Table S2). For the 140 K structure, which represents the I/C-CDW phase, the corresponding RMC-refined model was instead folded into a $1a \times 1a \times 2c$ tetragonal supercell, where *a* and *c* are derived from the PDFgui fit in Fig. 3(f). No local symmetry constraints were imposed on the atomic positions within the cell. The positions of the 76 atoms in the resulting unit cell (see Table S3) were defined by the geometric centers of the positions of equivalent atoms projected from the RMC configurations. This procedure preserves the experimentally determined tetragonal lattice parameters and the correlated component of the lattice distortions identified in Figs. 6 and 7. The calculations were performed within the framework of density functional theory using the generalized gradient approximation (GGA) with the Perdew-Burke-Ernzerhof (PBE) exchange-correlation functional, as implemented in the Vienna Ab initio Simulation Package (VASP)[65]. The projector-augmented wave (PAW) potential PAW_PBE Er_3 was used for Er, in which the strongly localized 4*f* electrons are treated as frozen core states and nine electrons with the $5p^6 5d^1 6s^2$ valence configuration were treated explicitly. Accordingly, no Hubbard-(U) correction was applied to the Er *4f* electrons. The PAW potentials for Ir and Si explicitly included their $5d^7 6s^2$ and $3s^2 3p^2$ states as valence electrons, respectively. A Hubbard correction of U = 2 eV was applied to the Ir 5 d states[66]. To assess the sensitivity of calculated electronic structure to this choice, additional calculations were performed using U = 0. A comparison of the total DOS obtained with U = 0 and U = 2 eV (Fig. S4) shows that the choice of U does not change the main conclusions of this study. The plane-wave basis energy cutoff was set to 480 eV. Brillouin-zone integrations were performed using a 4 × 4 × 8 Monkhorst-Pack (k)-point mesh for both the basic $1a \times 1a \times 1c$ unit cell and the $1a \times 1a \times 2c$ I/C-CDW model cells. A Gaussian smearing of 0.05 eV was used in the DOS calculations to provide sufficient resolution of the electronic states near the Fermi level while maintaining numerical convergence. Spin-orbit coupling was included self-consistently to account for relativistic effects, but it was found to have a negligible influence on the final results. A similar DFT computational protocol has been employed to assess the electronic structure of other CDW materials involving rare earth, 5*d* metal and Si species such as $Gd_2Os_3Si_5$[64]. Importantly, in contrast

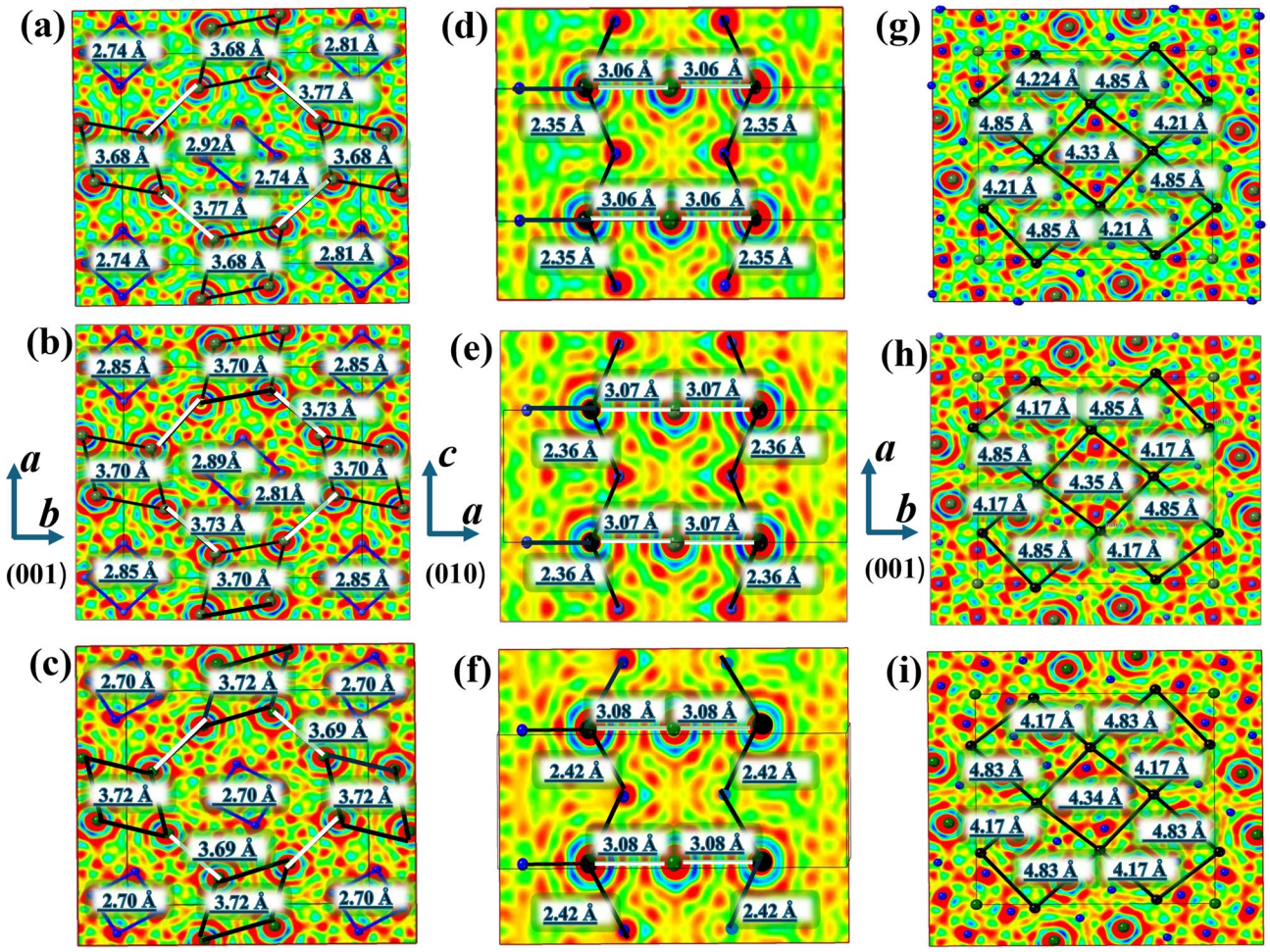


Fig. 6. Projections of the electron density distribution of $Er_5Ir_4Si_{10}$ onto the (001) and (010) atomic planes at (**a**, **d**,**g**) room temperature, (**b**, **e**,**h**) 180 K, and (**c**, **f**,**i**) 140 K. Er, Ir, and Si atoms are represented by green, black, and blue circles, respectively. In the (001) planes (**a**-**c**), the Si atoms form square-like motifs that gradually rotate with decreasing temperature. At room temperature and 180 K, these motifs are distorted, with long and short sides (black lines) of 2.92 and 2.74 Å, and 2.89 and 2.81 Å, respectively. At 140 K, the motifs become nearly uniform squares with a side length of 2.70 Å. Er atoms form rhombic motifs within the same planes. The corresponding Er-Er distances (black lines) increase from 3.68 Å at room temperature to 3.70 Å at 180 K and 3.72 Å at 140 K. In contrast, the distances between Er atoms located at the vertices of neighboring rhombuses (white lines) decrease from approximately 3.77 Å at room temperature to 3.69 Å at 140 K. In the (010) planes (d-f), Ir and Si atoms form zigzag chains. Along these chains, the Ir-Si distances increase from 2.35 Å at room temperature to 2.36 Å at 180 K and 2.42 Å at 140 K. The Er-Si distances (white lines) increase from 3.06 Å at room temperature to 3.08 Å at 140 K. The pattern of Ir-Ir distances in the (001) atomic planes also evolves with decreasing temperature (g-i). The shorter Ir-Ir distances decrease from 4.21 Å at room temperature to 4.17 Å at 140 K, while the longer Ir-Ir distances decrease from 4.85 Å to 4.83 Å, respectively. Each atomic position shown in panels (**a**, **b**,**d**, **e**,**g**, **h**) represents the geometric center of the positions of 576 corresponding atoms projected from the respective 22,000-atom RMC-refined models. Each atomic position shown in panels (**c**, **f**,**i**) represents the geometric center of the positions of 288 corresponding atoms projected from the respective 22,000-atom RMC-refined model. In both cases, no local crystallographic symmetry constraints were imposed on the atomic positions. As illustrated in the figure, the changes in interatomic distances are accompanied by a redistribution of the electron density, consistent with the presence of substantial electron-lattice interactions. Overall, the pattern of interatomic distances evolves with decreasing temperature due to lattice distortions associated with the emergence of CDW order. Notably, the 60 Å × 60 Å × 60 Å and 80 Å × 80 Å × 80 Å RMC models converged to patterns of interatomic distances that are virtually identical to those shown in panels (**a**-**i**). The uncertainty in all distances shown in the figure is ± 0.01 Å.

to conventional DFT studies, no additional structural optimization of the RMC-refined models was performed. That is because the DFT optimization significantly alters the RMC-refined structure for $Er_5Ir_4Si_{10}$, leading to poor agreement with the experimental PDF data and substantial differences in the calculated electronic band structure (see Fig. S3). The validity of this approach has been demonstrated in our recent PDF studies on $Lu_2Ir_3Si_5$, $NbTe_4$ and APt_2X_2 (A = U, Ce, or La; X = Si or Ge) CDW materials[46,48,67]. The computed band structures are shown in

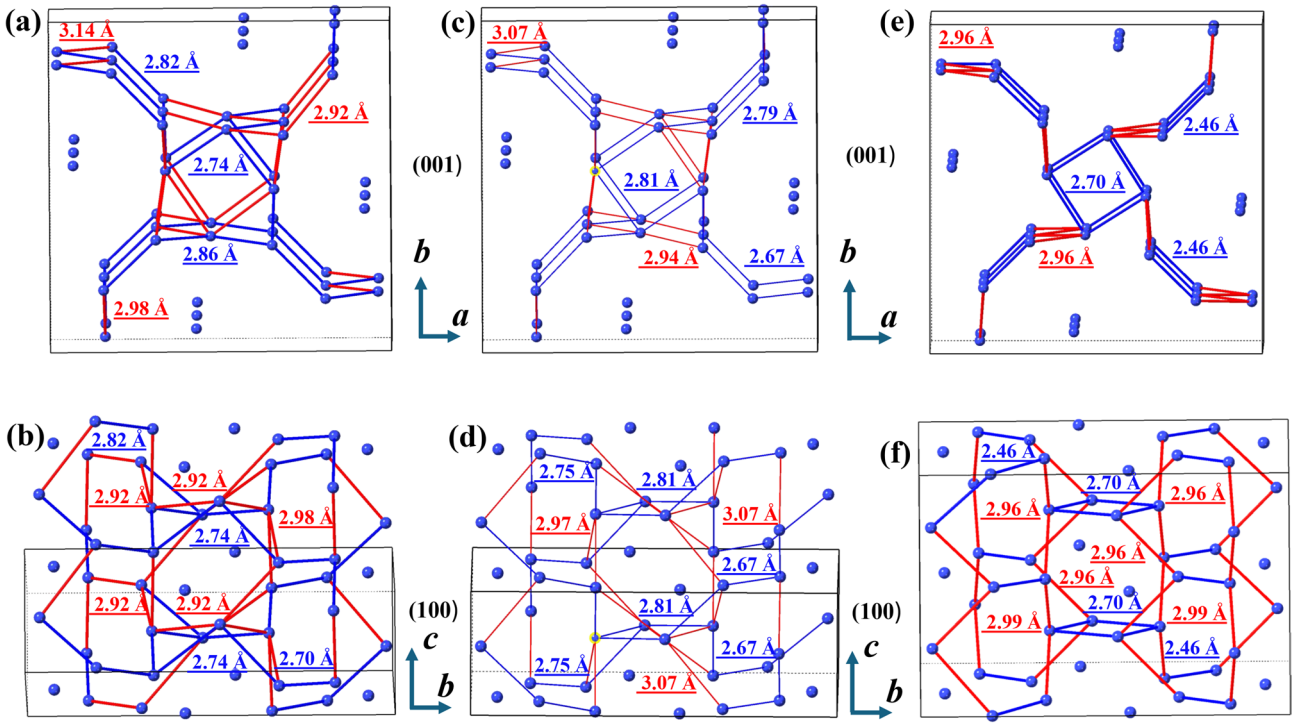


Fig. 7. Projection of the Si framework in $Er_5Ir_4Si_{10}$ onto the (001) and (100) atomic planes. Each atomic position shown in panels (**a**-**d**) represents the geometric center of the positions of 576 corresponding atoms projected from the 22,000-atom RMC models refined against PDF data obtained at 300 K and 180 K, respectively. In panels (**e**, **f**), each position represents the geometric center of the projected positions of 288 corresponding atoms in the 22,000-atom RMC models refined against PDF data obtained at 140 K. Si-Si distances shorter than 2.9 Å are shown in blue, while those in the 2.9–3.2 Å range are shown in red. The $1a \times 1a \times 1c$ cell in (a-d) and the $1a \times 1a \times 2c$ supercell in (**e**, **f**) are outlined with thin lines. Significant changes in Si-Si distances along the *a*, *b* and *c* directions of the crystal lattice are observed upon decreasing temperature. The uncertainty in all distances shown in the figure is ± 0.01 Å.

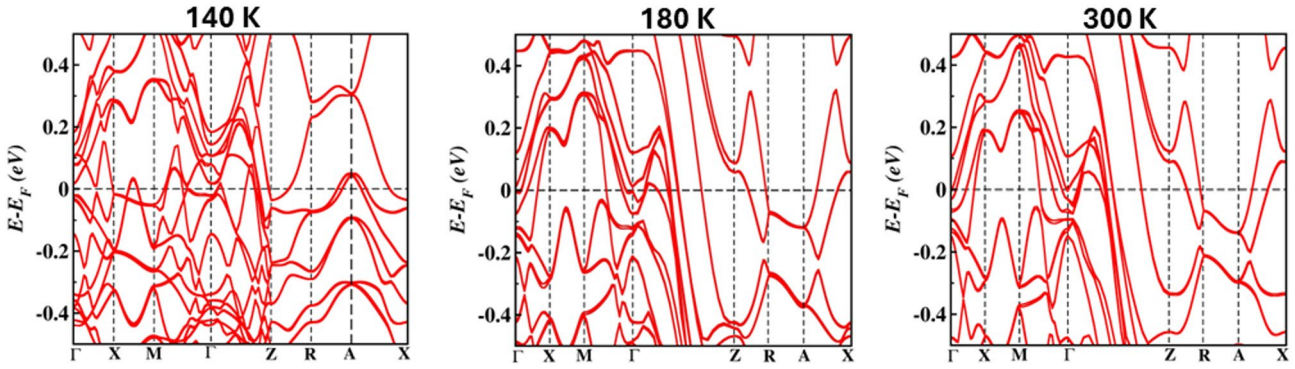


Fig. 8. Electronic band structures of tetragonal $Er_5Ir_4Si_{10}$ at 300 K, 180 K, and 140 K, shown along high-symmetry directions in the Brillouin zone. Calculations at 300 K and 180 K use $1a \times 1a \times 1c$ RMC-derived structural models, while the 140 K results are based on a $1a \times 1a \times 2c$ RMC-refined structural model.

Fig. 8. All exhibit metallic character, with electron and hole pockets present at the Fermi level. The corresponding total density of states (DOS) near the Fermi energy (E_f) is presented in Fig. 9. As shown, our structural models predict that the emergence of I/C-CDW order leads to a reduction in the DOS at E_F, consistent with muon relaxation time measurements[36], thereby supporting the reliability of our structural models. The DOS begins to decrease already in the CDW precursor phase and is further reduced upon the emergence of long-range I/C-CDW order. The reduced total DOS is consistent with the observed highly nonlinear evolution of the resistivity from room temperature to below $T_{\mathrm{I/C\text{-}CDW}}$.While further calculations of CDW-related properties are possible,

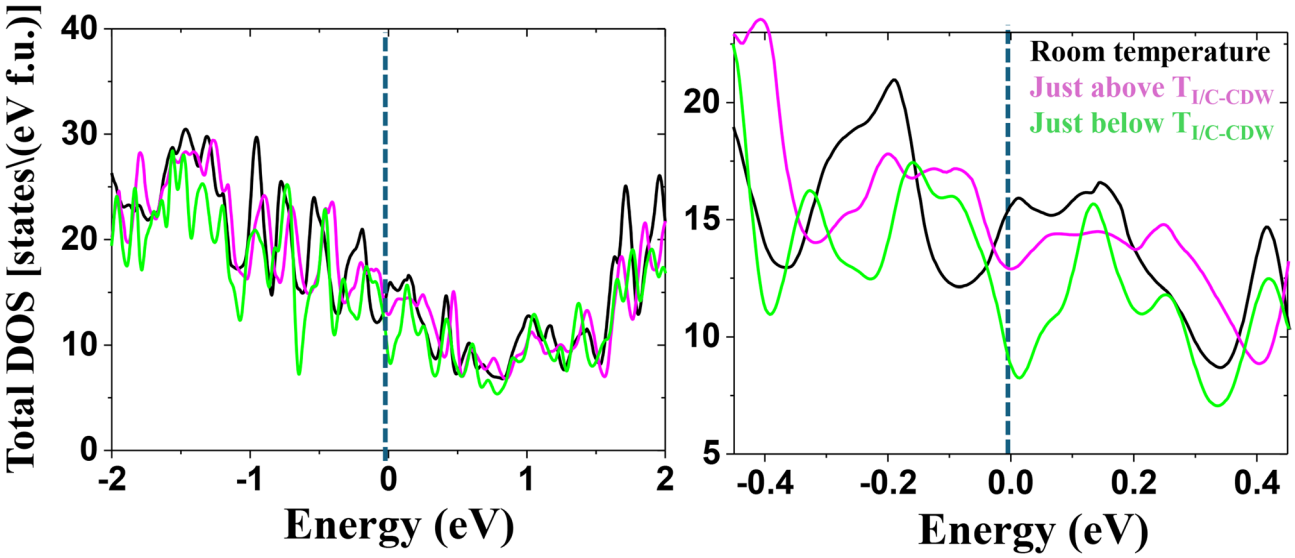


Fig. 9. Total electronic density of states (DOS) of $Er_5Ir_4Si_{10}$ calculated from RMC-refined structural models, shown over an extended energy range (left) and in the vicinity of the Fermi energy, E_f (vertical dashed line) (right), for 300 K (black), 180 K (magenta) and 140 K (green). Consistent with muon relaxation time measurements, the DOS is observed to decrease below $T_{I/C\text{-}CDW}$. The reduction appears to begin above this temperature, likely reflecting the onset of short-range lattice distortions before long-range I/C-CDW order emerges. The DOS are normalized per eV per formula unit (f.u.).

they are beyond the scope of the present work. To facilitate future computational studies of CDWs in $Er_5Ir_4Si_{10}$, we provide our structural models in Tables S1-S3 as Supplemental Material.

Phonon modes in $Er_5Ir_4Si_{10}$ from DFT calculations based on PDF-derived structural data

It is also well established that experimentally determined crystal structures can provide useful structural models for phonon calculations. Accordingly, the *1a x 1a x 2c* structural model used to calculate the electronic structure of the I/C-CDW phase was also employed to compute the corresponding phonon dispersion using the PHONOPY package[68]. The resulting phonon spectrum is shown in Fig. 10(a). The phonon dispersion of the I/C-CDW precursor phase above $T_{I/C-CDW}$ was similarly calculated using the *1a x 1a x 1c* structural model employed for the electronic-structure calculations at 180 K. The resulting phonon spectrum is shown in Fig. 10(b). As in the electronic-structure calculations, no additional structural optimization was performed for either model in order to retain the experimentally derived lattice distortions shown in Figs. 6 and 7. This is because DFT optimization significantly alters the RMC-refined structures of $Er_5Ir_4Si_{10}$, leading to poorer agreement with the experimental PDF data (Figs. S3(a, b) and S5(a, b)) and substantial differences in the calculated phonon dispersions (Fig. S5(c) vs. Fig. 10(a) and Fig. S6 vs. Fig. 10(b)). Accordingly, the imaginary phonon frequencies discussed below should be interpreted as features associated with the experimentally derived finite-temperature structures rather than with DFT-optimized ground-state structures.

A prominent feature of the phonon dispersion in the precursor CDW phase is the presence of phonon instabilities, manifested as imaginary (plotted as negative) frequencies, along the Γ-X-M and Z-R-A-Z high-symmetry paths in the Brillouin zone (Fig. 10(b)). In particular, the extended instability along Z-R-A-Z indicates a soft/unstable phonon manifold over a substantial portion of the q_Z =1/2 Brillouin-zone face, rather than an instability localized at a single high-symmetry point. Importantly, this manifold contains the Z=(0,0,1/2) wave vector, corresponding to the CDW modulation vector q_{C-CDW}=(0,0,1/2) determined by single-crystal X-ray diffraction experiments[23]. The phonon dispersion of the I/C-CDW phase also exhibits phonon instabilities, primarily along the Γ-X-M high-symmetry path in the Brillouin zone, with the strongest instability occurring near Γ, ((0,0,0)). In the reciprocal-space coordinates of the doubled $1a \times 1a \times 2c$ cell used to describe the I/C-CDW phase, Γ is equivalent, modulo a reciprocal-lattice vector, to (q=(0,0,1)), which corresponds to vector q_{C-CDW}=(0,0,1/2) in the single $1a \times 1a \times 1c$ cell used to describe the precursor CDW phase. Thus, the strongest phonon feature in the 140 K I/C-CDW structure occurs at the physical wave vector corresponding to the (Z)-point component of the extended q_Z =1/2 unstable manifold already present in the 180 K precursor structure. This systematic wave-vector correspondence suggests that the transition into the I/C-CDW phase can be viewed as a selection of the Z=(0,0,1/2) component from a pre-existing soft q_Z =1/2 manifold, thereby retaining the characteristic modulation along the (c) direction while establishing the specific CDW ordering observed below $T_{I/C-CDW}$. Such persistence and wave-vector selection may also be relevant to the further evolution of the CDW state upon cooling toward T_{C-CDW}. Furthermore, the broad Kohn-like dips[69] in the calculated phonon dispersion, together with the small resistivity anisotropy and the absence of a sharp metal-insulator transition at $T_{I/C-CDW}$, are consistent with the three-dimensional character of the lattice modulations in $Er_5Ir_4Si_{10}$ revealed by our study.

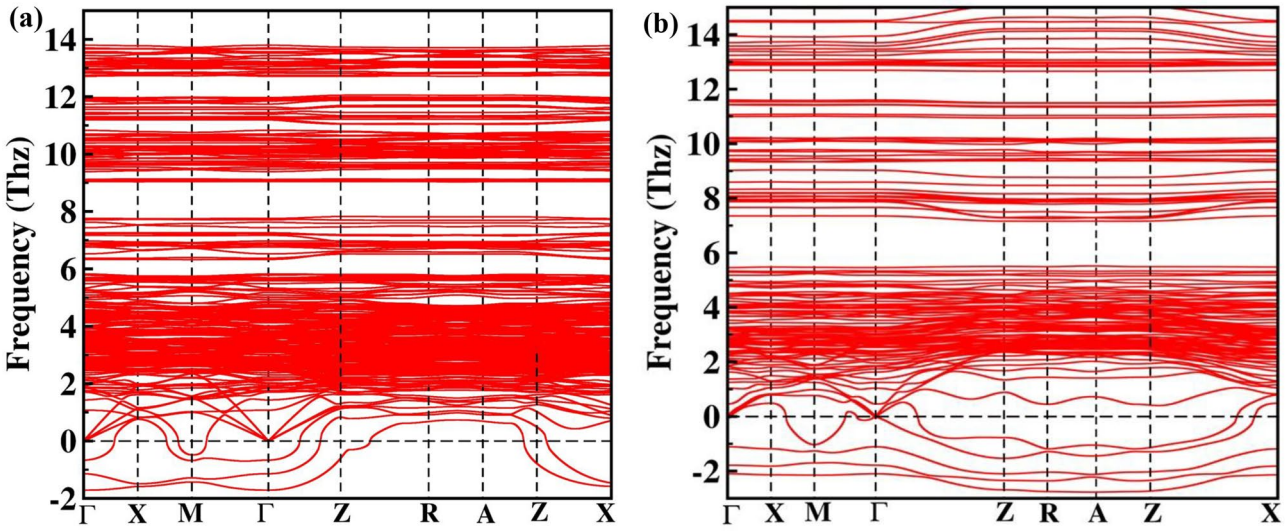


Fig. 10. **(a)** Phonon spectrum computed for an unoptimized $1a \times 1a \times 2c$ unit cell of $Er_5Ir_4Si_{10}$ at 140 K, derived from the large-scale RMC model described in the text. The spectrum is plotted along a selected high-symmetry path in the Brillouin zone of the $1a \times 1a \times 2c$ cell; Γ, X, M, Z, R, and A denote the corresponding high-symmetry q-points. Phonon instabilities, indicated by negative frequencies, are observed along the Γ-X-M high-symmetry path. The strongest instability (lowest negative value) occurs near the Γ point, $q = (0,0,0)$, which is equivalent, modulo a reciprocal-lattice vector, to $q = (0,0,1)$ in the reciprocal-space coordinates of the $1a \times 1a \times 2c$ cell. **(b)** Phonon spectrum computed for an unoptimized $1a \times 1a \times 1c$ unit cell of $Er_5Ir_4Si_{10}$ at 180 K, derived from the large-scale RMC model described in the text. The spectrum is plotted along a selected high-symmetry path in the Brillouin zone of the cell; Γ, X, M, Z, R, and A denote the corresponding high-symmetry points. Phonon instabilities, indicated by negative frequencies, are observed along the Γ-X and Z-R-A-Z high-symmetry paths. In particular, the extended instability along Z-R-A-Z reveals a soft/unstable phonon manifold over a substantial portion of the q_z=1/2 Brillouin-zone face. This manifold includes the Z=(0,0,1/2) point, corresponding to the experimentally observed CDW modulation vector $q_{C\text{-}CDW}$ = (0,0,1/2). In the reciprocal-space coordinates of the doubled cell, Z=(0,0,1/2) corresponds to the same physical $q = (0,0,1)$ wave vector identified in the independently derived 140 K structural model. Thus, the 180 K precursor state already exhibits an extended lattice instability containing the wave vector that becomes dominant upon entering the I/C-CDW phase. This correspondence suggests that the transition selects the (Z)-point component from a pre-existing soft q_z =1/2 manifold, preserving its characteristic modulation along the (c) direction while establishing the specific CDW ordering observed below the transition.

Broad Kohn-like features in the phonon dispersion have also been reported for other three-dimensional CDW systems containing rare-earth, 5(d)-metal, and Si species, such as $LaPt_2Si_2$[70,71].

Conclusions

In summary, our study demonstrates that $Er_5Ir_4Si_{10}$ exhibits lattice distortions already above $T_{I/C\text{-}CDW}$, below which coexisting incommensurate and commensurate CDWs emerge. These distortions involve displacements of Er, Ir, and Si atoms from their room-temperature crystallographic positions, with particularly pronounced distortions involving the Si atoms. As the temperature decreases, the atomic displacements become increasingly correlated, leading to a substantial reorganization of the local bonding network and the development of long-range lattice and charge-density modulations below $T_{I/C\text{-}CDW}$. At the same time, the spatial distribution of the electron density evolves with temperature, consistent with substantial electron-lattice interactions.

DFT calculations based directly on the experimentally derived structural models reveal an extended soft/unstable phonon manifold along the q_z=1/2 Brillouin-zone face in the precursor phase, which includes the $q_{C\text{-}CDW}$=(0,0,1/2) CDW modulation wave vector previously identified by single-crystal X-ray diffraction experiments. Upon entering the I/C-CDW phase, the strongest phonon feature occurs at the equivalent physical wave vector in the doubled structural cell. This wave-vector correspondence suggests that the CDW transition involves selection of the Z=(0,0,1/2) component from a pre-existing soft q_z=1/2 manifold, while retaining the characteristic modulation along the (c) direction. Consistent with experimental observations, the calculations also predict a partial reduction of the electronic density of states at the Fermi level upon the emergence of CDW order. Together, these results support the reliability of the CDW structural information obtained from PDF analysis and reveal a close connection between precursor lattice distortions, wave-vector selection, and the unusual electronic properties of $Er_5Ir_4Si_{10}$.

The findings reported here are likely relevant to other members of the $RE_5Ir_4Si_{10}$ family and are consistent with our recent studies of the $RE_2Ir_3Si_5$[48] and $RENiC_2$[47] families of CDW materials, further supporting the idea that local lattice distortions may contribute significantly to the emergence of CDW order in three-dimensional quantum materials. More broadly, the experimental and computational framework demonstrated here—

combining element-specific total X-ray scattering with large-scale structural modeling and DFT calculations based on experimentally derived structures—provides a useful approach for uncovering subtle lattice distortions and their coupling to electronic degrees of freedom[72].

Data availability

X-ray diffraction data are available at the Harvard Dataverse (2025), https://doi.org/10.7910/DVN/B9WA63. Additional data are available from the corresponding author upon reasonable request.

Received: 9 July 2026; Accepted: 22 September 2026
Published online: 29 September 2026

References

1. Rossnagel, K. On the origin of charge-density waves in select layered transition-metal dichalcogenides. *J. Phys.: Condens. Matter* **23**, 213001 (2011).
2. Zhu, X., Guo, J., Zhang, J. & Plummer, E. W. Misconceptions associated with the origin of charge density waves. *Adv. Phys. : X*. **2**, 622 (2017).
3. van Smaalen, S. The Peierls transition in low-dimensional electronic crystals. *Acta Crystallogr. Sect. A: Found. Adv. A*. **61**, 51 (2005).
4. Monceau, P. Electronic crystals: An experimental overview. *Adv. Phys.* **61**, 325 (2012).
5. Chen, C. W., Choe, J. & Morosan, E. Charge density waves in strongly correlated electron systems. *Rep. Prog. Phys.* **79**, 084505 (2016).
6. Greene, L. H., Thompson, J. & Schmalian, J. Strongly correlated electron systems—reports on the progress of the field. *Rep. Prog Phys.* **80**, 030401 (2017).
7. Lee, P. A., Nagaosa, N. & Wen, X. G. Doping a Mott insulator: Physics of high-temperature superconductivity. *Rev. Mod. Phys.* **78**, 17 (2006).
8. Alvarado, S. J. G. et al. Frustrated ising charge correlations in the kagome metal ScV_6Sn_6. *Phys. Rev. B* **110**, L140304 (2024).
9. Fradkin, E., Kivelson, S. A. & Tranquada, J. M. Colloquium: Theory of intertwined orders in high temperature superconductors. *Rev. Mod. Phys.* **87**, 457 (2015).
10. Ortiz, B. R. et al. CsV_3Sb_5: AZ_2 topological kagome metal with a superconducting ground state. *Phys. Rev. Lett.* **125**, 247002 (2020).
11. Roman, M., Strychalska-Nowak, J., Klimczuk, T. & Kolincio, K. K. Extended phase diagram of RNiC2 family: Linear scaling of the Peierls temperature. *Phys. Rev. B* **97**, 041103(R) (2018).
12. Prathiba, G. et al. Tuning the ferromagnetic phase in the CDW compound $SmNiC_2$ via chemical alloying. *Sci. Rep.* **6**, 26530 (2016).
13. Maeda, H., Kondo, R. & Nogami, Y. Multiple charge density waves compete in ternary rare-earth nickel carbides, $RNiC_2$ (R: Y, Dy, Ho, and Er). *Phys. Rev. B*. **100**, 104107 (2019).
14. Rogl, P. Chap. 51: Phase equilibria in ternary and higher order systems with rare earth elements and silicon, in Handbook of Physics and Chemistry of Rare Earths, edited by K. A. J Gschneidner, and L. Eyring (Amsterdam: North-Holland, (1984).
15. Braun, H. F. & Segre, C. U. The superconductivity of $Sc_5T_4Si_{10}$ (T = Co, Rh, Ir) and isomorphous compounds. *Solid State Commun.* **35**, 735 (1980).
16. Becker, B. et al. Strongly coupled charge-density wave transition in single-crystal $Lu_5Ir_4Si_{10}$. Phys. *Rev. B*. **59**, 7266 (1999).
17. van Smaalen, S. et al. Multiple charge-density waves in $R_5Ir_4Si_{10}$ (R = Ho, Er, Tm and Lu). *Phys. Rev. B*. **69**, 014103 (2004).
18. Shelton, R. N. et al. Electronic phase transition and partially gapped fermi surface in superconducting $Lu^5Ir^4Si^{10}$. *Phys. Rev. B* **34**, 4590 (1986).
19. Lue, C. S. et al. Thermal hysteresis in the charge-density-wave transition of $Lu_5Rh_4Si_{10}$. Phys. *Rev. B*. **66**, 033101 (2002).
20. Yang, H. D., Klavins, P. & Shelton, R. N. Low-temperature physical properties of $R_5Ir_4Si_{10}$ (R = Dy, Ho, Er, Tm, and Yb) compounds. *Phys. Rev. B*. **43**, 7688 (1991).
21. Kuo, Y. K. et al. Ionic size and atomic disorder effects on the charge-density-wave transitions in $R_5Ir_4Si_{10}$ (R = Dy-Lu). *Phys. Rev. B*. **67**, 195101 (2003).
22. Lee, M. H. et al. Concomitant charge-density-wave and unit-cell-doubling structural transitions in $Dy_5Ir_4Si_{10}$. *Phys. Rev. B* **89**, 195142 (2014).
23. Galli, F. et al. Charge-density-wave transitions in the local-moment magnet $Er_5Ir_4Si_{10}$. *Phys. Rev. Lett.* **85**, 158 (2000).
24. Kuo, Y. K., Lue, C. S., Hsu, F. H., Li, H. H. & Yang, H. D. Thermal properties of $Lu_5Ir_4Si_{10}$ near the charge-density-wave transition. *Phys. Rev. B*. **64**, 125124 (2001).
25. Singh, Y., Nirmala, R., Ramakrishnan, S. & Malik, S. K. Competition between superconductivity and charge-density-wave ordering in the $Lu_5Ir_4(Si_{1-x}Ge_x)_{10}$ alloy system, Phys. Rev. B 72, 045106 (2005). (2005).
26. Leroux, M., Rodière, P. & Opagiste, C. Charge density wave and superconducting properties in single crystals of $Lu_5Ir_4Si_{10}$. *J. Supercond. Nov. Magn.* **26**, 1669 (2012).
27. Yang, H. D., Klavins, P. & Shelton, R. N. Competition between superconductivity and charge- density-waves in the pseudoternary system $(Lu_{1-x}Sc_x)_5Ir_4Si_{10}$. *Phys. Rev. B*. **43**, 7681 (1991).
28. Hossain, Z. et al. Coexistence of magnetic order and charge density wave in a kondo lattice: $Yb_5Ir_4Si_{10}$. *Phys. Rev. B*. **71**, 060406 (2005).
29. Galli, F. et al. Coexistence of charge density wave and antiferromagnetism in $Er_5Ir_4Si_{10}$. *J. Phys. : Condens. Matter*. **14**, 5067 (2002).
30. Galli, F. et al. Magnetic structure of the Er^{3+} moments in the charge-density-wave compound $Er_5Ir_4Si_{10}$. *Phys. Rev. B* **62**, 13840 (2000).
31. Tseng, C. M., Chen, C. H. & Yang, H. D. Direct observation of charge-density waves in $Ho_5Ir_4Si_{10}$. *Phys. Rev. B* **77**, 155131 (2008).
32. Ghosh, K., Ramakrishnan, S. & Chandra, G. Magnetism in the $R_5Ir_4Si_{10}$ (R = Ho and Er) systems. *Phys. Rev. B*. **48**, 4152 (1993).
33. Galli, R. et al. Resistivity anomalies and local moment magnetism in $Er_5Ir_4Si_{10}$ single crystal. *Phys. B Condens. Matter*. **281-282**, 171 (2000).
34. Tsutsumia, K., Nimori, S. & Kido, G. Direct observation of remarkable crystalline-electric-field effect in quasi-two-dimensional antiferromagnet $Er_5Ir_4Si_{10}$ single crystal by low-temperature specific heat. *J. Alloys Compd.* **480**, 35 (2009).
35. Ramakrishnan, S. & van Smaalen, S. Unusual ground states in $R_5T_4X_{10}$ (R= rare earth; T = Rh, Ir; and X = Si, Ge, Sn): a review, Rep. *Prog Phys.* **80**, 116501 (2017).
36. Galli, F. et al. μSR studies on the charge density waves in $RE_5Ir_4Si_{10}$. *Phys. B: Condens. Matter*. **319**, 282 (2002).
37. Ong, N. P. & Brill, J. W. Conductivity anisotropy and transverse magnetoresistance of $NbSe_3$. *Phys. Rev. B* **18**, 5265 (1978).
38. Jung, M. H., Kim, C. H., Migliori, A., Galli, F. & Mydosh, J. A. Magnetic-field and pressure effects on charge-density-wave, superconducting, and magnetic states in $Lu_5Ir_4Si_{10}$ and $Er_5Ir4Si10$. *Phys. Rev. B* **68**, 132102 (2003).
39. Supplementary & Material.
40. Grüner, G. *Density Waves in Solids* (Addison-Wesley, 1994).
41. Wilson, J. A., Di Salvo, F. J. & Mahajan, S. Charge-density waves and superlattices in the metallic layered transition metal dichalcogenides. *Adv. Phys.* **24**, 117 (1975).

42. Malliakas, C. D. & Kanatzidis, M. G. A double charge density wave in the single tellurium square net in $Cu_{0.63}EuTe_2$. *J. Am. Chem. Soc.* **131**, 6896 (2009).
43. Egami, T. & Billinge, S. J. L. *Underneath the Bragg Peaks: Structural Analysis of Complex Materials* (Pergamon, 2003).
44. Kim, H. J. et al. Local atomic structure and discommensurations in the charge density wave of $CeTe_3$. *Phys. Rev. Lett.* **96**, 226401 (2006).
45. Petkov, V., Chapagain, K., Shastri, S. & Ren, Y. Genesis of the periodic lattice distortions in the charge density wave state of 2H-$TaSe_2$. *Phys. Rev. B.* **101**, 121114 (2020).
46. Petkov, V. et al. Charge density wave order, local lattice distortions, and topological electronic states in $NbTe_4$. *Phys. Rev. B.* **108**, 174112 (2023).
47. Petkov, V. et al. Close-up view of the interplay between lattice distortions and charge density waves: Case study on rare-earth nickel carbides. *Phys. Rev. B* **112**, 184107 (2025).
48. Petkov, V., Zafar, A., Jakhar, M., Abeykoon, A. M. M. & Hegedüs, Z. Three-dimensional lattice modulations in the charge density wave system $Lu_2Ir_3Si_5$. *Phys. Rev. B* **112**, 224108 (2025).
49. Bozin, E. S. et al. Crystallization of polarons through charge and spin ordering transitions in 1T-TaS_2. *Nat. Commun.* **14**, 7055 (2023).
50. Juhás, P., Davis, T., Farrow, C. L. & Billinge, S. J. L. PDFgetX3: a rapid and highly automatable program for processing powder diffraction data into total scattering pair distribution functions. *J. Appl. Crystallogr.* **46**, 560 (2013).
51. Klug, H. P. & Alexander, L. E. X-ray Diffraction Procedures for Polycrystalline and Amorphous Materials, edited by A. J. EdwardsWiley, New York, (1974).
52. Waseda, Y. (ed.) *Novel Application of Anomalous (Resonance) X-ray Scattering for Structural Characterization of Disordered Materials* (Springer, 1984).
53. Petkov, V. et al. Application of differential resonant high-energy X-ray diffraction to three-dimensional structure studies of nanosized materials: A case study of Pt-Pd nanoalloy catalysts, Acta Crystallogr. *Sec A: Found. Adv.* **74**, 553 (2018).
54. Shastri, S. D. Combining flat crystals, bent crystals, and compound refractive lenses for high-energy x-ray optics. *J. Synchrotron Rad.* **11**, 150 (2004).
55. Petkov, V. RAD, a program for analysis of x-ray diffraction data from amorphous materials for personal computers. *J. Appl. Crystallogr.* **22**, 387 (1989).
56. Toby, B. H. & Von Dreele, R. B. GSAS-II: the genesis of a modern open-source all purpose crystallography software package. *J. Appl. Crystallogr.* **46**, 544 (2013).
57. Petkov, V., Zafar, A., Jakhar, M. & Abeykoon, A. M. M. Genesis and atomic structure of the charge density wave phase of 1T-VSe_2. *Phys. Rev. B* **111**, 014105 (2025).
58. Amin, R., Pandey, J., Beyer, K. & Petkov, V. Two-step charge density wave transition and hidden transient phase in 1T-$TiSe_2$. *Phys. Rev. B* **109**, 144106 (2024).
59. Petkov, V., Baumbach, R., Abeykoon, A. M. M. & Mydosh, J. A. Three-dimensional charge density wave in the dual heavy fermion system UPt_2Si_2. *Phys. Rev. B* **107**, 245101 (2023).
60. Farrow, C. L. et al. PDFfit2 and PDFgui: Computer programs for studying nanostructure in crystals. *J. Phys.: Condens. Matter* **19**, 335219 (2007).
61. Keen, D. A., Tucker, M. G. & Dove, M. T. Reverse Monte Carlo modelling of crystalline disorder. *J. Phys. : Condens. Matter*. **17**, S15 (2005).
62. Petkov, V., Zafar, A., Gallington, L., Shastri, S. & Aoun, B. Structural phase diagram for Sm- substituted $BiFeO_3$ multiferroics. *Rev. Mater.* **8**, 124407 (2024).
63. Aoun, B. Fullrmc, a rigid body reverse monte carlo modeling package enabled with machine learning and artificial intelligence. *J. Comput. Chem.* **37**, 1102 (2016).
64. Sharma, V. et al. Room temperature charge density wave in a tetragonal polymorph of $Gd_2Os_3Si_5$ and study of its origin in the $RE_2T_3X_5$ (RE= Rare earth, T= Transition metal, X = Si, Ge) series. *Chem. Mater.* **36**, 6888 (2024).
65. Kresse, G. & Furthmüller, J. Efficient iterative schemes for ab initio total-energy calculations using a plane-wave basis set. *Phys. Rev. B.* **54**, 11169 (1996).
66. Tesch, R. & Kowalski, P. M. Hubbard U parameters for transition metals from first principles. *Phys. Rev. B* **105**, 195153 (2022).
67. Nocerino, E. et al. Multiple unconventional charge density wave transitions in $LaPt_2Si_2$ superconductor clarified with high-energy X-ray diffraction. *Commun. Mater.* **4**, 77 (2023).
68. Togo, A., Oba, F. & Tanaka, I. First-principles calculations of the ferroelastic transition between rutile-type and $CaCl_2$-type SiO_2 at high pressures. *Phys. Rev. B* **78**, 134106 (2008).
69. Kohn, W. Image of the Fermi surface in the vibration spectrum of a metal. *Phys. Rev. Lett.* **2**, 393 (1959).
70. Kim, S., Kim, K. & Min, B. I. The mechanism of charge density wave in Pt-based layered superconductors: $SrPt_2As_2$ and $LaPt_2Si_2$. *Sci. Rep.* **5**, 15052 (2015).
71. Petkov, V. et al. Local lattice distortions and electronic orders in strongly correlated systems by resonant total x-ray scattering: A case study of APt_2X_2 intermetallics (A = U, Ce, or La and X = Si or Ge). *Phys. Rev. B.* **108**, 224110 (2023).
72. Zafar, A. X-ray diffraction data for $Er_5Ir_4Si_{10}$, Harvard Dataverse (2025). https://doi.org/10.7910/DVN/B9WA63

Acknowledgements

This research was supported by the U.S. Department of Energy, Office of Science, Office of Basic Energy Sciences under Award DE-SC0021973 and performed on APS beam time award (https://doi.org/10.46936/APS-189912/60014025) from the Advanced Photon Source, a U.S. Department of Energy (DOE) Office of Science user facility operated for the DOE Office of Science by Argonne National Laboratory under Contract No. DE-AC02-06CH11357. This research used 28-ID-1 beamline of the National Synchrotron Light Source, a U. S. Department of Energy (DOE) office of Science User Facility operated for the DOE Office of Science by Brookhaven National Laboratory under Contract No. DE-SC0012704. PARAM Rudra, a national supercomputing facility at Inter-University Accelerator Centre (IUAC), New Delhi, was used to obtain the DFT results presented in this paper.

Author contributions

V. Petkov, (A) Zafar, S. Shastri, L. Gallington and AM Milinda Abeykoon participated in the experiments. M. Jakhar performed the DFT calculations. (B) Aoun contributed to the structure modeling. V. Petkov wrote the manuscript text. All authors reviewed the manuscript.

Funding

Not applicable.

Declarations

Competing interests
The authors declare no competing interests.

Additional information
Supplementary Information The online version contains supplementary material available at https://doi.org/10.1038/s41598-026-73228-w.

Correspondence and requests for materials should be addressed to V.P.

Reprints and permissions information is available at www.nature.com/reprints.

Publisher's note Springer Nature remains neutral with regard to jurisdictional claims in published maps and institutional affiliations.

Open Access This article is licensed under a Creative Commons Attribution-NonCommercial-NoDerivatives 4.0 International License, which permits any non-commercial use, sharing, distribution and reproduction in any medium or format, as long as you give appropriate credit to the original author(s) and the source, provide a link to the Creative Commons licence, and indicate if you modified the licensed material. You do not have permission under this licence to share adapted material derived from this article or parts of it. The images or other third party material in this article are included in the article's Creative Commons licence, unless indicated otherwise in a credit line to the material. If material is not included in the article's Creative Commons licence and your intended use is not permitted by statutory regulation or exceeds the permitted use, you will need to obtain permission directly from the copyright holder. To view a copy of this licence, visit http://creativecommons.org/licenses/by-nc-nd/4.0/.

© The Author(s) 2026